

First-principles analysis of in-plane anomalous Hall effect using symmetry-adapted Wannier Hamiltonians and multipole decomposition

Hiroto Saito and Takashi Koretsune

^a*Department of Physics, Tohoku University, Aoba-ku, Sendai, 980-8578, Japan*

Abstract

The in-plane anomalous Hall effect occurs when magnetization lies within the same plane as the electric field and Hall current, and requires magnetic point groups lacking rotational or mirror symmetries. While it is observed in both Weyl semimetals and elemental ferromagnets, the microscopic role of higher-order multipoles remains unclear. Here, we develop a microscopic framework that combines time-reversal-symmetric Wannier functions with a symmetry-adapted multipole basis to decompose the first-principles Wannier Hamiltonian into electric, magnetic, magnetic toroidal, and electric toroidal multipoles. This approach allows us to rotate the magnetization rank by rank and quantify how each multipole affects the conductivity. Applying this framework to body-centered cubic iron, we find that high-rank magnetic and magnetic toroidal multipoles contribute with magnitudes comparable to magnetic dipoles, while magnetic toroidal 16-poles act with the opposite sign. Furthermore, based on this multipole analysis, we apply uniaxial strain along the [103] direction to control the dominant multipoles contributing to the conductivity. The strain substantially modifies its angular dependence, demonstrating that multipole-resolved Hamiltonian engineering and magnetoelastic control serve as practical routes to predict and tune the in-plane anomalous Hall conductivity in simple ferromagnets.

Keywords: In-plane anomalous Hall effect, Wannier functions, Density functional theory

1. Introduction

The anomalous Hall effect (AHE) is a transverse transport phenomenon in systems with broken time-reversal symmetry [1, 2]. Traditionally, AHE has been understood as a response proportional to the magnetization, where the Hall current flows perpendicular to the plane defined by the magnetization and the electric field. However, in recent years, Berry-curvature-based formulations and symmetry analyses have significantly extended this conventional picture. In particular, many theoretical and experimental studies have shown that AHE can appear even in systems without a net magnetization, such as Mn_3X ($X=Ir, Sn, Ge, Pt, Rh$) [3, 4, 5, 6, 7, 8, 9, 10, 11, 12] and altermagnets [13, 14, 15, 16], where multipolar magnetic order or other time-reversal-odd quantities play an essential role.

Along with these developments, the in-plane anomalous Hall effect (IAHE) has attracted attention recently [17, 18, 19, 20, 21, 22, 23, 24, 25, 26, 27, 28]. IAHE refers to an anomalous Hall current that flows within the plane spanned by the magnetization and the electric field. Compared with the conventional AHE geometry, IAHE requires an additional magnetic point-group symmetry constraint [19, 22]. Therefore, its observation can provide further information on low-symmetry magnetic order and on topological band structures induced by spin-orbit coupling (SOC).

Initial experimental studies of IAHE focused on materials combining strong SOC with topological band structures. Hall responses consistent with IAHE have been reported in Weyl semimetals and related systems such as $EuCd_2Sb_2$ [23], Cd_3As_2 [24], $SrRuO_3$ [26], and $Co_3Sn_2S_2$ [27]. These observations were attributed to mechanisms such as effective out-of-plane magnetization components induced by orbital magnetization, or Weyl-point splitting mediated by Berry curvature [23]. More recently, IAHE has also been confirmed even in simple cubic ferromagnets such as Fe and Ni [25].

Particularly in cubic systems, a theoretical study predicted that octupolar terms can cause the AHE vector to deviate from the magnetization direction through higher-order spin-orbit perturbations [28]. Although this approach successfully explains the angular dependence of IAHE, it relies on a phenomenological expansion with respect to the spin magnetization, and does not explicitly connect the microscopic terms related to higher-order multipoles or orbital magnetism. Therefore, a microscopic treatment based on first-principles-derived models is expected to provide complementary and essential insights from the viewpoint of multipoles.

To quantify the IAHE as well as AHE in realistic material, a tight-binding Hamiltonian from first-principles calculations is useful. Maximally localized Wannier functions (MLWFs) are widely used for this purpose, as they enable accurate band interpolation and model construction from density functional theory (DFT) by combining subspace disentanglement [29] with spread minimization [30]. More recent extensions preserve key physical quantities by, for example, optimizing Wannier functions with respect to their projectability onto pseudo-atomic orbitals [31], constructing Wannier functions closest to atomic orbitals [32, 33], or employing symmetry-adapted Wannier functions (SAWF) that enforce site-symmetry constraints [34, 35]. For ferromagnets, we previously developed SAWF and introduced the time-reversal symmetric Wannier (TRS-Wannier) method, which combines TR-symmetric gauge fixing with spin-group symmetry constraints to capture the angular dependence of magnetic anisotropy energy with high accuracy [36]. In parallel, a symmetry-adapted multipole basis (SAMB) enables decomposition of Hermitian operators into electric, magnetic, magnetic toroidal, and electric toroidal types classified by rank and the point-group irreducible representations [37, 38, 39, 33, 40].

Here, we combine the TRS-Wannier with SAMB analysis to quantitatively evaluate the symmetry of Hamiltonians derived from first-principles calculations. This approach enables us to elucidate the microscopic origins of the IAHE in ferromagnets. In bcc Fe, we analyze the angular dependence of the anomalous Hall conductivity (AHC) under magnetization rotation by comparing theoretical formulas, DFT calculations, and multipole models.

2. Method

2.1. In-plane anomalous Hall effect

We evaluate intrinsic AHC using linear response theory [2]. Current density J_i is given by

$$J_i = \sigma_{ij} E_j, \quad (1)$$

$$\sigma_{ij} = -\frac{e^2}{\hbar} \int_{\text{BZ}} \frac{d^3k}{8\pi^3} \Omega_{ij}(\mathbf{k}), \quad (2)$$

$$\Omega_{ij}(\mathbf{k}) = -2\hbar^2 \text{Im} \sum_n^{\text{occ.}} \sum_m^{\text{unocc.}} \frac{\langle \psi_{n\mathbf{k}} | v_i | \psi_{m\mathbf{k}} \rangle \langle \psi_{m\mathbf{k}} | v_j | \psi_{n\mathbf{k}} \rangle}{(\varepsilon_{n\mathbf{k}} - \varepsilon_{m\mathbf{k}})^2}, \quad (3)$$

where i, j label Cartesian components, \mathbf{E} is the applied electric field, $\varepsilon_{n\mathbf{k}}$ and $\psi_{n\mathbf{k}}$ are the band energy eigenvalues and Bloch eigenstates at wave vector \mathbf{k} , and $v_i = (1/\hbar) \partial H / \partial k_i$ is the velocity operator. Here, σ_{ij} is an antisymmetric tensor ($\sigma_{ij} = -\sigma_{ji}$).

The anomalous Hall vector $\boldsymbol{\sigma}$ is defined as the pseudovector $\sigma_k = \frac{1}{2} \epsilon_{ijk} \sigma_{ij}$, namely,

$$\boldsymbol{\sigma} = (\sigma_{yz}, \sigma_{zx}, \sigma_{xy}). \quad (4)$$

If the magnetization direction $\hat{\mathbf{M}}$ is oriented along a high-symmetry direction, $\boldsymbol{\sigma}$ is constrained to be parallel to it. One can verify that $\boldsymbol{\sigma}$ transforms as a pseudovector. That is, when we consider rotation matrices, $R_{ij} \in \text{SO}(3)$, σ_{ij} transforms as

$$\sigma'_{ij} = R_{ip} R_{jq} \sigma_{pq}, \quad (5)$$

and thus, we can obtain

$$\begin{aligned} \sigma'_k &= \frac{1}{2} \epsilon_{kij} R_{ip} R_{jq} \sigma_{pq} \\ &= \frac{1}{2} \det(R) R_{kr} \epsilon_{rpq} \sigma_{pq} \\ &= \det(R) R_{kr} \sigma_r. \end{aligned} \quad (6)$$

Here, we have used the following identity relation for rotation matrices:

$$\epsilon_{kij} R_{ip} R_{jq} = \det(R) R_{kr} \epsilon_{rpq}. \quad (7)$$

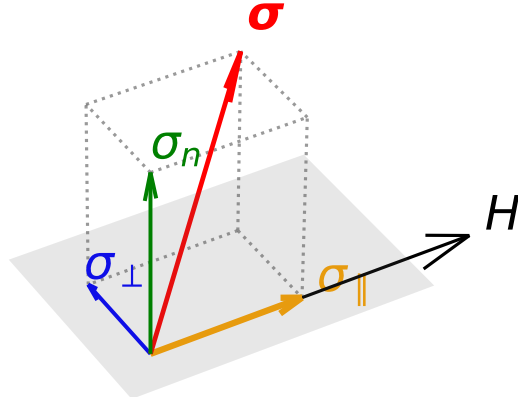


Figure 1: Decomposition of the anomalous Hall vector $\boldsymbol{\sigma}$ into the components parallel to the magnetization (σ_{\parallel}), in-plane perpendicular (σ_{\perp}), and out-of-plane (σ_n). The gray plane represents the plane formed by rotating \mathbf{H} .

We decompose $\boldsymbol{\sigma}$ into three components with respect to the magnetization direction $\hat{\mathbf{M}}$. When the magnetization rotates within a plane with unit normal \mathbf{n} , we define the in-plane unit vector orthogonal to $\hat{\mathbf{M}}$ as $\mathbf{e}_\perp = \mathbf{n} \times \hat{\mathbf{M}}$. The components are then

$$\sigma_{\parallel} = \boldsymbol{\sigma} \cdot \hat{\mathbf{M}}, \quad (8)$$

$$\sigma_{\perp} = \boldsymbol{\sigma} \cdot \mathbf{e}_\perp, \quad (9)$$

$$\sigma_{\mathbf{n}} = \boldsymbol{\sigma} \cdot \mathbf{n}. \quad (10)$$

Here, σ_{\parallel} corresponds to the conventional AHC, while σ_{\perp} and $\sigma_{\mathbf{n}}$ represent the IAHE components (Fig. 1). In the experiment, the measurement direction of $\boldsymbol{\sigma}$ is fixed while the magnetization is rotated. As a result, σ_{\parallel} and σ_{\perp} rotate with the magnetization, whereas the direction of $\sigma_{\mathbf{n}}$ remains invariant. For example, when the magnetization rotates by angle ψ in the xy plane, the components transform as

$$\begin{pmatrix} \sigma_{\parallel} \\ \sigma_{\perp} \\ \sigma_{\mathbf{n}} \end{pmatrix} = \begin{pmatrix} \cos \psi & \sin \psi & 0 \\ -\sin \psi & \cos \psi & 0 \\ 0 & 0 & 1 \end{pmatrix} \begin{pmatrix} \sigma_{yz} \\ \sigma_{zx} \\ \sigma_{xy} \end{pmatrix} = \begin{pmatrix} \sigma_{\mathbf{e}_{\perp},z} \\ \sigma_{z,\hat{\mathbf{M}}} \\ \sigma_{xy} \end{pmatrix}. \quad (11)$$

Therefore, it is possible to measure the magnetization-rotation dependence only of $\sigma_{\mathbf{n}}$.

The magnetization-direction dependence of $\boldsymbol{\sigma}$ is phenomenologically expanded in terms of multipoles in spin space [28]:

$$\boldsymbol{\sigma} = p_{ij} \hat{M}_j \mathbf{e}_i + o_{ijkl} \hat{M}_j \hat{M}_k \hat{M}_l \mathbf{e}_i + \dots, \quad (12)$$

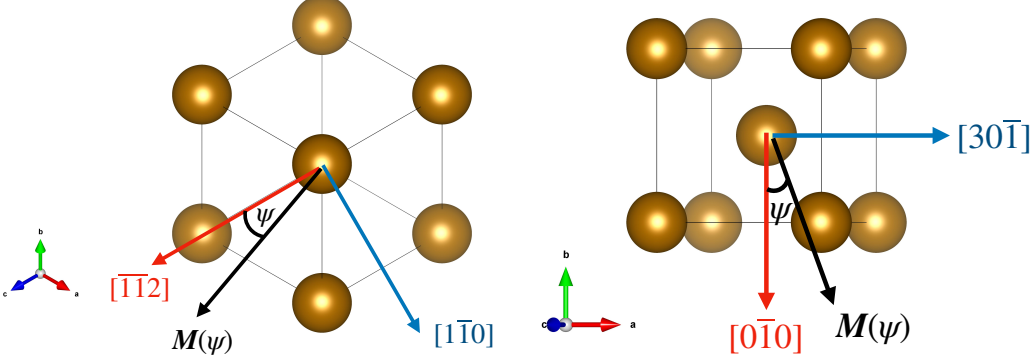
$$p_{ij} = \frac{3}{4\pi} \int \sin \theta d\phi \sigma_i(\theta, \phi) \hat{M}_j \quad (13)$$

$$o_{ijkl} = \frac{7}{8\pi} \int \sin \theta d\phi \sigma_i(\theta, \phi) [5\hat{M}_j \hat{M}_k \hat{M}_l - \hat{M}_j \delta_{kl} - \hat{M}_k \delta_{jl} - \hat{M}_l \delta_{jk}], \quad (14)$$

where \mathbf{e}_i is the unit vector along the i -th Cartesian axis. For cubic-symmetric systems, this reduces to

$$\boldsymbol{\sigma} = \alpha \begin{pmatrix} M_x \\ M_y \\ M_z \end{pmatrix} + \beta \begin{pmatrix} M_x^3 \\ M_y^3 \\ M_z^3 \end{pmatrix}, \quad (15)$$

with $\alpha = p_{xx} - \frac{3}{2}o_{xxxx}$ and $\beta = \frac{5}{2}o_{xxxx}$. Based on this expression, we derive the angular dependence of σ_{\parallel} , σ_{\perp} , and $\sigma_{\mathbf{n}}$ for magnetization rotation in the (111) and (103) planes (Fig. 2).



(a) Magnetization rotation within the (111) plane from $[1\bar{1}2]$ to $[1\bar{1}0]$.
(b) Magnetization rotation within the (103) plane from $[0\bar{1}0]$ to $[30\bar{1}]$.

Figure 2: Schematic definitions of the magnetization rotation planes and the azimuthal angle ψ .

For a rotation by angle ψ , angle-dependence of each component is given as follows:

- (111) plane rotation from $[\bar{1}\bar{1}2] \rightarrow [\bar{1}\bar{1}0]$

$$\sigma_{\parallel} = \alpha + \frac{\beta}{2}, \quad (16)$$

$$\sigma_{\perp} = 0, \quad (17)$$

$$\sigma_{\mathbf{n}} = \frac{\sqrt{6}}{6} \beta \cos 3\psi. \quad (18)$$

- (103) plane rotation from $[0\bar{1}0] \rightarrow [30\bar{1}]$

$$\sigma_{\parallel} = \alpha + \beta \left(\frac{273}{400} + \frac{9}{100} \cos 2\psi + \frac{91}{400} \cos 4\psi \right), \quad (19)$$

$$\sigma_{\perp} = -\frac{\beta}{400} (18 \sin 2\psi + 91 \sin 4\psi), \quad (20)$$

$$\sigma_{\mathbf{n}} = \frac{6\beta}{25} \sin^3 \psi. \quad (21)$$

2.2. Symmetry-adapted multipole basis

We construct SAMB to represent all electronic degrees of freedom with a complete and orthonormal basis. SAMB is defined as the direct product

of atomic multipole $\mathbb{X}^{(a)}$ that describes atomic orbital parts and site/bond-cluster multipole $\mathbb{Y}^{(s/b)}$ that corresponds to sublattices or bonding clusters [41, 37]. Specifically,

$$\begin{aligned} & \mathbb{Z}(l, \Gamma, n, \gamma | s, k) \\ &= \sum_{\substack{\Gamma_1, n_1, \gamma_1 \\ \Gamma_2, n_2, \gamma_2}} C(X, Y | Z) \mathbb{X}^{(a)}(l_1, \Gamma_1, n_1, \gamma_1 | s, k) \otimes \mathbb{Y}^{(s/b)}(l_2, \Gamma_2, n_2, \gamma_2), \end{aligned} \quad (22)$$

where l is rank, Γ is the space group irreducible representation, n is multiplicity, γ is the component index within irreducible representation (e.g., u, v for E representation, x, y, z for T representation), s indicates spin degrees of freedom ($s = 0$ or 1), k represents spin components ($k = 0$ for $s = 0$ and $k = -1, 0, 1$ for $s = 1$), and $C(X, Y | Z)$ is the Clebsch-Gordan coefficient. These indices are omitted when redundant, and we sometimes collectively denote the set of indices by i .

Each multipole is classified as one of four types according to its transformation properties under time-reversal and spatial-inversion symmetries: electric (\mathbb{Q}), magnetic (\mathbb{M}), magnetic toroidal (\mathbb{T}), and electric toroidal (\mathbb{G}). SAMB is orthonormal and complete, satisfying

$$\langle \mathbb{Z}_i | \mathbb{Z}_j \rangle = \text{tr}[\mathbb{Z}_i^\dagger \mathbb{Z}_j] = \delta_{ij}, \quad (23)$$

$$\left[\sum_i |\mathbb{Z}_i\rangle \langle \mathbb{Z}_i| \right]_{aa', bb'} = \sum_i [\mathbb{Z}_i]_{aa'} [\mathbb{Z}_i^*]_{bb'} = \delta_{ab} \delta_{a'b'}. \quad (24)$$

This enables unique decomposition of the Hamiltonian H , with multipole decomposition defined as

$$H^{\text{MD}} = \sum_i z_i \mathbb{Z}_i, \quad (25)$$

$$z_i = \text{tr}[\mathbb{Z}_i^\dagger H], \quad (26)$$

where coefficient z_i represents contributions from each multipole component.

For quantitative evaluation of symmetry preservation of Wannier Hamiltonians, we define energy eigenvalue differences before and after decomposition as

$$\Delta_{\text{energy}} = \frac{1}{N_{\mathbf{k}} N_{\text{W}}} \sum_{n\mathbf{k}} |\varepsilon_{n\mathbf{k}} - \varepsilon_{n\mathbf{k}}^{\text{MD}}|, \quad (27)$$

where $N_{\mathbf{k}}$ denotes the number of \mathbf{k} -points sampled in the Brillouin zone, N_{W} is the number of Wannier bands, and $\varepsilon_{n\mathbf{k}}^{\text{MD}}$ is the energy eigenvalue of H^{MD} .

2.3. Time-reversal symmetric Wannier method and multipole rotation

We use the TRS-Wannier method for a high-precision analysis of the AHE during magnetization rotation. Expanding the Hamiltonian into a multipole basis and introducing rank-wise rotation operations enables a quantitative evaluation of the contribution of each multipole component to the AHC. This section describes specific formulation and definitions of rotation operations.

In the TRS-Wannier method, Wannier function basis preserves time-reversal symmetry during Wannierization [36]. Choosing a spin-quantization axis perpendicular to the magnetization (e.g., take $x \perp z$) makes the $S_x = \pm \frac{1}{2}$ Wannier functions identical in real space, because site symmetries relate the two spin states. For example, in cubic crystals a C_{2z} rotation acts similarly to time reversal for an in-plane axis. As a result, the two spins share the same centers and spreads and form time-reversal-symmetric pairs.

We also apply spin group symmetry constraints to the Hamiltonian [42, 43, 28]. The ferromagnetic spin group is the direct product of spin-only group $\infty 2'$ and crystal point group, justified in the negligible SOC limit. Decomposing the Hamiltonian into time-reversal symmetric and antisymmetric parts yields:

$$\begin{aligned} H^{\text{MD}} &= H^s + H^a \\ &= \left(\sum_i q_i \mathbb{Q}_i + \sum_i g_i \mathbb{G}_i \right) + \left(\sum_i m_i \mathbb{M}_i + \sum_i t_i \mathbb{T}_i \right). \end{aligned} \quad (28)$$

Since SOC is time-reversal symmetric, it belongs to the first term H^s . The second term H^a represents the Hamiltonian without SOC and should satisfy spin-only group symmetry. From the Hermiticity of the Hamiltonian, H^a can generally be written as

$$H^a = iA_0 + \mathbf{A} \cdot \mathbf{s}, \quad (29)$$

where $\mathbf{s} = (s_x, s_y, s_z)$ is the Pauli matrix vector.

The spin-only group $\infty 2'$ consists of spin rotations $C_{\psi z}^s$ around the z -axis (magnetization direction) with arbitrary angle ψ ($0 \leq \psi < 2\pi$), composite operations TC_{2x}^s combining spin rotation about x -axis, C_{2x}^s , with time reversal operation, T , and their products, forming a continuous group. The constraint imposed by $C_{\psi z}^s$ symmetry gives $A_x = A_y = 0$, while the constraint by TC_{2x}^s yields $A_0 = 0$. Therefore, H^a is limited to

$$H^a = A_z s_z, \quad (30)$$

i.e., only the magnetization direction component.

Next, let us consider the spin rotation for the TRS Hamiltonian. The TRS Hamiltonian that includes only the s_z component in H^a is expressed as,

$$H^{\text{TRS}} = \left(\sum_i q_i \mathbb{Q}_i + \sum_i g_i \mathbb{G}_i \right) + \text{tr} \left[s_z^\dagger \left(\sum_i m_i \mathbb{M}_i + \sum_i t_i \mathbb{T}_i \right) \right] s_z, \quad (31)$$

where the trace is taken over spin space. Using the spinor rotation matrix

$$U^s(\theta, \phi) = \begin{pmatrix} \cos \theta/2 & e^{-i\phi} \sin \theta/2 \\ -e^{i\phi} \sin \theta/2 & -\cos \theta/2 \end{pmatrix}, \quad (32)$$

we can rotate magnetization from z -axis to general direction (θ, ϕ) , and obtain $H^{\text{TRS}}(\theta, \phi)$ as

$$\begin{aligned} H^{\text{TRS}}(\theta, \phi) = & \left(\sum_i q_i \mathbb{Q}_i + \sum_i g_i \mathbb{G}_i \right) \\ & + \text{tr} \left[s_z^\dagger \left(\sum_i m_i \mathbb{M}_i + \sum_i t_i \mathbb{T}_i \right) \right] \begin{pmatrix} \cos \theta & e^{-i\phi} \sin \theta \\ e^{i\phi} \sin \theta & -\cos \theta \end{pmatrix}. \end{aligned} \quad (33)$$

For the rank- l multipole rotation, we define the Hamiltonian with only the rank- l multipole components rotated, $H_l^{\text{TRS}}(\theta, \phi)$, as

$$\begin{aligned} H_l^{\text{TRS}}(\theta, \phi) = & \left(\sum_i q_i \mathbb{Q}_i + \sum_i g_i \mathbb{G}_i \right) \\ & + \text{tr} \left[s_z^\dagger \left(\sum_{i \in \text{rank } l} m_i \mathbb{M}_i + \sum_{i \in \text{rank } l} t_i \mathbb{T}_i \right) \right] \begin{pmatrix} \cos \theta & e^{-i\phi} \sin \theta \\ e^{i\phi} \sin \theta & -\cos \theta \end{pmatrix}. \end{aligned} \quad (34)$$

2.4. Calculation details

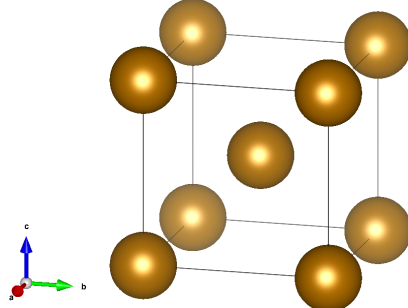


Figure 3: Crystal structures of body-centered cubic iron (bcc Fe).

We performed first-principles calculations using the QUANTUM ESPRESSO package [44, 45] with a plane-wave basis set and pseudopotential methods. The resulting electronic structures were used to construct tight-binding models via the SYMWANNIER program [35]. For bcc Fe (space group No. 229), the lattice constant was set to $a = 2.868 \text{ \AA}$ (Fig. 3). The plane-wave energy cutoffs for the wave functions and the charge density were 64.0 Ry and 782.0 Ry, respectively. Exchange-correlation effects were treated within the Perdew-Burke-Ernzerhof (PBE) generalized gradient approximation (GGA) [46]. Ultrasoft pseudopotentials from PSLIBRARY [47] were employed. SOC was included in the non-self-consistent field calculations, and the Fermi energy used in all subsequent analyses was taken from this step.

Wannierization was carried out in a one-shot procedure, projecting onto localized s , p , and d orbitals at atomic sites, resulting in 36 spinor Wannier functions per atom. An $8 \times 8 \times 8$ k -mesh was used, corresponding to 59 inequivalent k points under symmetry. The inner energy window for disentanglement was chosen to include all $3d$ states. Importantly, the spin quantization axis during Wannierization was set perpendicular to the magnetization direction obtained from first-principles calculations. This ensured differences in Wannier centers of less than 10^{-6} \AA and differences in spreads of less than 10^{-8} \AA^2 for all up/down spinor pairs.

SAMB operators were generated with the MULTIPIE program [37]. We constructed operators for all irreducible representations and included bond terms through the 35th-nearest neighbor, thereby covering every bond present in the Wannier Hamiltonian. Retaining the full set of irreducible represen-

tations ($A_{1g} \oplus A_{2g} \oplus E_g \oplus T_{1g} \oplus T_{2g} \oplus A_{1u} \oplus A_{2u} \oplus E_u \oplus T_{1u} \oplus T_{2u}$) yields a total of 345,708 SAMB matrices.

AHC calculations were conducted with the WANNIERBERRI code [48]. Starting from a uniform 10^6 k -mesh, we performed 20 adaptive interpolation loops with a refinement factor of 50. The final calculations used approximately $N_k \approx 1.32 \times 10^8$ k points, confirming convergence.

3. Result

3.1. Multipole decomposition of Hamiltonians and analysis of dominant components

3.1.1. Evaluation of Hamiltonians using Symmetry-adapted multipole basis

We verify the completeness of the multipole decomposition of the TRS-Wannier Hamiltonian using the SAMB framework. Including multipoles up to the 35th-nearest neighbors ensures that the band structure converges to the DFT results (Fig. 4).

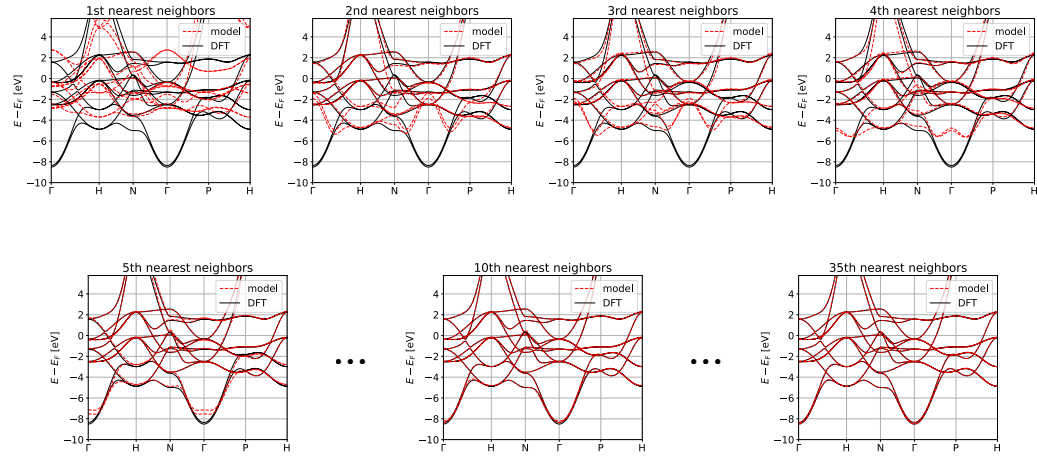


Figure 4: Dependence of the band structure on the bond range. Considering neighbors up to the 35th-nearest neighbors leads to convergence with the DFT results.

Beyond completeness, it is important to verify which irreducible representations actually appear in the Hamiltonian, as this substantiates the physical soundness of the decomposition. In this case, angular momentum operators \mathbf{L} and \mathbf{S} belong to T_{1g} representation. The bilinear, $\mathbf{L} \cdot \mathbf{S}$, decomposes as $T_{1g} \otimes T_{1g} = A_{1g} \oplus E_g \oplus T_{2g}$. Therefore, besides A_{1g} and T_{1g} , the Hamiltonian can contain E_g and T_{2g} components as well. Table 1 summarizes the

energy difference between the original and multipole decomposed Hamiltonians, Δ_{energy} , defined in Eq. (27). Here, we consider Wannier Hamiltonians obtained by the original Wannier90 and the TRS-Wannier methods introduced in Sec. 2.3. To check this convergence reliably, we modified both the original Wannier90 and the TRS-Wannier codes so that the output precision was increased to 16 digits after the decimal point. The first row corresponds to the multipole decomposition only using $A_{1g} \oplus T_{1g}$, the minimal set containing the identity and primary magnetic components. The second row adds the SOC-induced E_g and T_{2g} representations generated by $T_{1g} \otimes T_{1g}$. Including E_g and T_{2g} reduces Δ_{energy} to the order of 10^{-12} eV for TRS-Wannier, yielding an almost fully reconstructed Hamiltonian. TRS-Wannier attains about three orders of magnitude better symmetry-preserving accuracy than ordinary Wannier90 for the truncated physically motivated set, confirming the effectiveness of the symmetry constraints. SAMB thus provides a quantitative metric for Hamiltonian symmetry fidelity and a physically interpretable pathway for systematic improvement.

Table 1: Comparison of multipole decomposition reproduction accuracy between ordinary Wannier90 method and TRS-Wannier method.

Irreducible representation	Δ_{energy} [eV]	
	Wannier90	TRS-Wannier
$A_{1g} \oplus T_{1g}$	1.595×10^{-5}	1.607×10^{-5}
$A_{1g} \oplus T_{1g} \oplus E_g \oplus T_{2g}$	1.415×10^{-9}	2.024×10^{-12}

3.1.2. Multipole decomposition coefficients and physical interpretation

We extract the highest-magnitude coefficients from the multipole decomposition of the TRS-Wannier Hamiltonian. Figure 5 shows the top twenty coefficients, indicating that the dominant contributions are mostly electric multipoles Q belonging to the identity representation A_{1g} . Among the leading terms, z_{86479} ($M(1, T_{1g}, , 0|1, -1)$) is a T_{1g} magnetic dipole that constitutes the primary magnetic-ordering component of the Fe 3d orbitals.

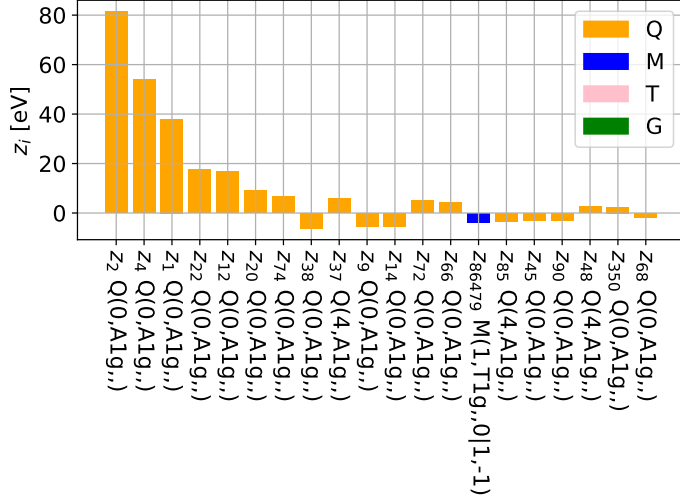


Figure 5: Top 20 coefficients in multipole decomposition of TRS-Wannier Hamiltonian.

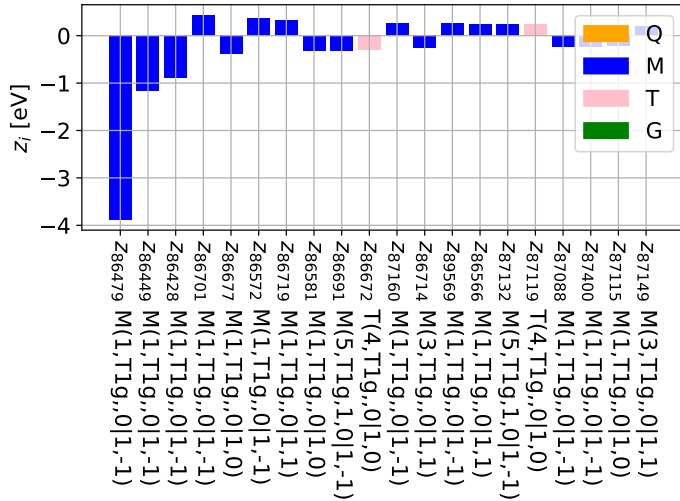


Figure 6: Top 20 coefficients in multipole decomposition of TRS-Wannier Hamiltonian (excluding electric multipoles Q).

Figure 6 shows the twenty largest coefficients in the multipole decomposition with electric multipoles excluded, thereby highlighting the leading

magnetic order. It is reasonable that they all belong to the same T_{1g} representation as magnetization. The three largest non-electric contributions— z_{86479} , z_{86449} , and z_{86428} —share the same factorization:

$$\mathbb{M}(1, T_{1g}, , 0|1, -1) = \mathbb{M}^{(a)}(1, T_{1g}, , 0|1, -1) \otimes \mathbb{Q}^{(s)}(0, A_{1g}, ,). \quad (35)$$

Here, the atomic multipole $\mathbb{M}^{(a)}$ represents the components of magnetic dipoles arising from the d , p , and s orbitals, whereas the site-cluster electric monopole $\mathbb{Q}^{(s)}$ represents an intra-atomic contribution (Fig. 7). In other words, these correspond to exchange splitting term, $J_z\sigma_z$, for d , p , and s orbitals.

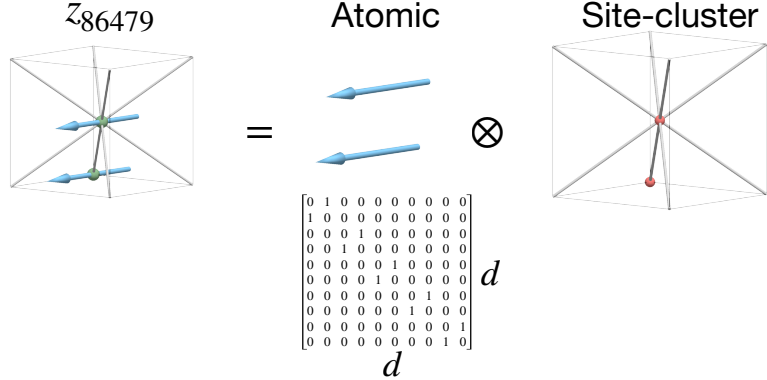


Figure 7: Schematic of SAMB z_{86479} ($\mathbb{M}(1, T_{1g}, , 0|1, -1)$). The atomic magnetic dipole represents the magnetization-direction components of the d orbitals, whereas the site-cluster electric monopole represents an intra-atomic contribution. All figures of schematic multipoles were prepared with QTDRAW [37].

By contrast, the coefficient of the fourth-largest magnetic-dipole in Fig. 6, z_{86701} ($\mathbb{M}(1, T_{1g}, , 0|1, -1)$), has a different factorization:

$$\mathbb{M}(1, T_{1g}, , 0|1, -1) = \mathbb{G}^{(a)}(4, T_{2u}, , 0|1, -1) \otimes \mathbb{T}^{(b)}(3, A_{2u}, ,). \quad (36)$$

Here, the atomic multipole corresponds to electric-toroidal 16-pole \mathbb{G} involving the p and d orbitals, while the bond-cluster multipole describes magnetic-toroidal octupole hopping \mathbb{T} that is purely imaginary on nearest-neighbor bonds (Fig. 8). Thus, even in bcc Fe, nearest-neighbor p - d hopping accompanied by simultaneous spin- and orbital-changes is appreciable.

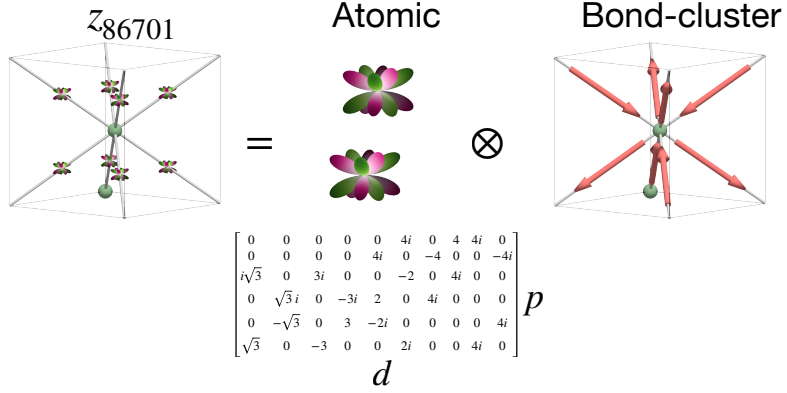


Figure 8: Schematic view of SAMB z_{86701} ($\mathbb{M}(1, T_{1g}, , 0|1, -1)$). The atomic electric-toroidal 16-pole \mathbb{G} represents p - d order, while the bond-cluster magnetic-toroidal octupole \mathbb{T} corresponds to purely imaginary nearest-neighbor hopping.

Consistent with this interpretation, Fig. 6 shows sizable magnetic-toroidal multipole \mathbb{T} among the largest non-electric coefficients. For example, magnetic-toroidal 16-pole z_{86672} ($\mathbb{T}(4, T_{1g}, , 0|1, 0)$) can be written as

$$\begin{aligned}
\mathbb{T}(4, T_{1g}, , 0|1, 0) = & \frac{\sqrt{5}}{4} \mathbb{Q}^{(a)}(3, T_{1u}, , 1|1, 0) \otimes \mathbb{T}^{(b)}(1, T_{1u}, , 2) \\
& - \frac{\sqrt{5}}{4} \mathbb{Q}^{(a)}(3, T_{1u}, , 2|1, 0) \otimes \mathbb{T}^{(b)}(1, T_{1u}, , 1) \\
& - \frac{\sqrt{3}}{4} \mathbb{Q}^{(a)}(3, T_{2u}, , 1|1, 0) \otimes \mathbb{T}^{(b)}(1, T_{1u}, , 2) \\
& - \frac{\sqrt{3}}{4} \mathbb{Q}^{(a)}(3, T_{2u}, , 2|1, 0) \otimes \mathbb{T}^{(b)}(1, T_{1u}, , 1). \quad (37)
\end{aligned}$$

Similarly, the atomic electric octupole \mathbb{Q} represents p - d order, while the bond-cluster magnetic-toroidal dipole \mathbb{T} corresponds to purely imaginary nearest-neighbor hopping (Fig. 9).

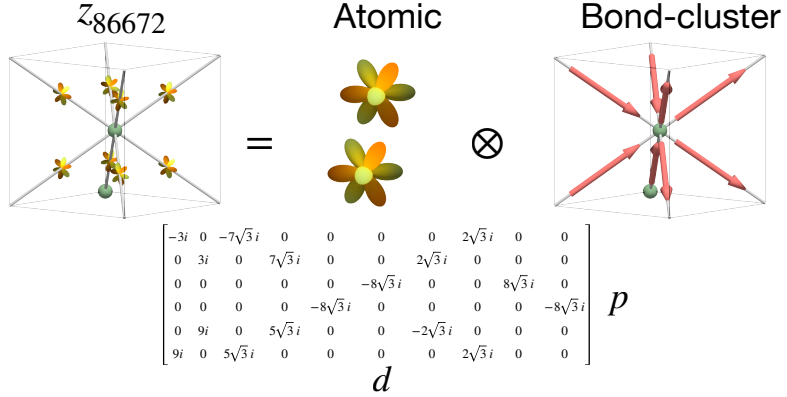


Figure 9: Schematic view of SAMB z_{86672} ($\mathbb{T}(4, T_{1g}, , 0|1, 0)$). The atomic electric octupole \mathbb{Q} couples with the bond-cluster magnetic-toroidal dipole \mathbb{T} , corresponding to purely imaginary nearest-neighbor hopping.

Beyond the nearest-neighbor terms, second-nearest-neighbor contributions are also evident in Fig. 6. For example, z_{87119} ($\mathbb{T}(4, T_{1g}, , 0|1, 0)$) factorizes in the same way as in Eq. (37), with the bond-cluster component corresponding to magnetic-toroidal hopping on second-nearest-neighbor bonds (Fig. 10).

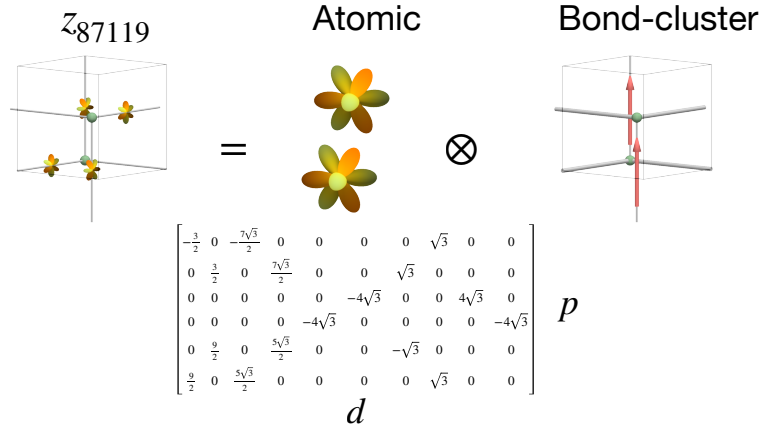


Figure 10: Schematic view of SAMB z_{87119} ($\mathbb{T}(4, T_{1g}, , 0|1, 0)$). The atomic electric octupole \mathbb{Q} couples with the bond-cluster magnetic-toroidal dipole \mathbb{T} , corresponding to purely imaginary second-nearest-neighbor hopping.

3.2. AHC angular dependence by rotation of magnetic and magnetic toroidal multipoles

3.2.1. Magnetization rotation and AHC angular dependence in (111) plane

Figure 11 shows the angular dependence of the AHC components, σ_{\parallel} , σ_{\perp} , and σ_n , during magnetization rotation in the (111) plane. Here, the AHC values are obtained from two approaches: (i) direct Wannierization at each magnetization angle (DFT-based) and (ii) the multipole rotation of the TRS-Wannier Hamiltonian (model-based). The theoretical angular dependencies given in Eqs. (16-18) are also plotted, where the parameters are fitted using the model-based results. The fitted values are $\alpha = -894.308$ and $\beta = 105.758$ [S/cm].

First, we find that the DFT and model-based results are in good agreement, indicating that the TRS-Wannier method successfully reproduces the angle-dependent Hamiltonian and can be applied to the AHC calculation. Regarding the angular dependence, the out-of-plane component σ_n (Fig.11(c)) reproduces the periodicity of the theoretical formula $\sigma_n = \frac{\sqrt{6}}{6} \beta \cos 3\psi$. However, parallel component σ_{\parallel} (Fig.11(a)) and perpendicular component σ_{\perp} (Fig.11(b)) show significant deviations from theoretical formulas with discernible 6ψ oscillation periods. Such 6ψ oscillations are clearly expected from the crystal symmetry and should be explained by higher-order terms that are neglected in Eq. (15).

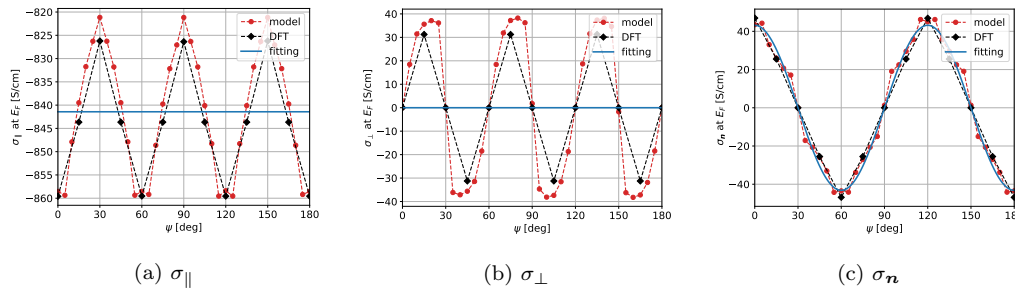


Figure 11: Angular dependence of AHC components (σ_{\parallel} , σ_{\perp} , σ_n) during magnetization rotation in the (111) plane. Symbols denote the results from DFT and TRS-Wannier calculations, while solid lines represent the fitted theoretical formulas ($\sigma_{\parallel} = \alpha + \frac{\beta}{2}$, $\sigma_{\perp} = 0$, $\sigma_n = \frac{\sqrt{6}}{6} \beta \cos 3\psi$), with fitting parameters $\alpha = -894.308$ and $\beta = 105.758$ [S/cm].

3.2.2. Magnetization rotation and AHC angular dependence in (103) plane

Figure 12 shows the angular dependence of the AHC components, σ_{\parallel} , σ_{\perp} , and σ_n , during magnetization rotation in the (103) plane. As in the (111)

case, symbols denote the results from DFT-based Wannierization at each magnetization angle and from the TRS-Wannier multipole-rotation model, while solid lines represent the theoretical formulas in Eqs. (19-21), with parameters fitted to the model-based results. The fitted values are $\alpha = -896.116$ and $\beta = 100.928$ [S/cm].

For the parallel component σ_{\parallel} (Fig.12(a)) and perpendicular component σ_{\perp} (Fig.12(b)), periods and phases nearly match theoretical formula $\sigma_{\parallel} = \alpha + \beta \left(\frac{273}{400} + \frac{9}{100} \cos 2\psi + \frac{91}{400} \cos 4\psi \right)$ and $\sigma_{\perp} = -\frac{\beta}{400} (18 \sin 2\psi + 91 \sin 4\psi)$, showing the model reproduces main angular dependence features. Since the fitted values of α and β are consistent between the (111) plane case and the present case, the low-order parameters are robust against surface orientations. However, in this case, the out-of-plane component σ_n (Fig.12(c)) shows two local minima at $\phi = 0^\circ$ and 90° which cannot be reproduced by the theoretical formula, $\sigma_n = \frac{6}{25} \beta \sin^3 \psi$. A similar valley-like feature near $\psi = 90^\circ$ has also been suggested by an experiment [25]. These deviations indicate that a low-order expansion in magnetization angle is insufficient for the (103) plane as well. We address higher-order and magnetic-toroidal contributions to the AHC in the next section.

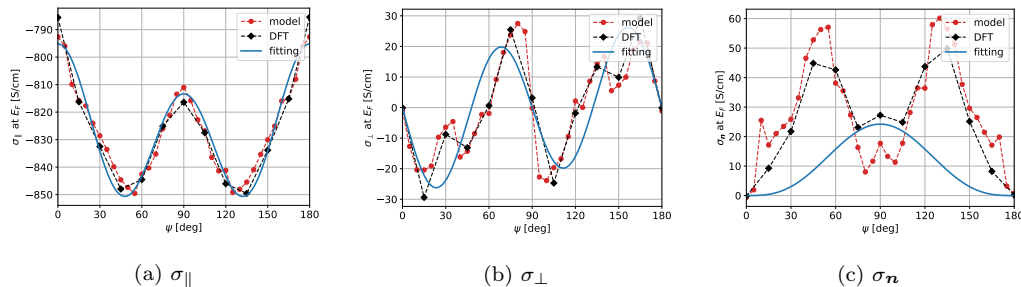


Figure 12: Angular dependence of AHC components (σ_{\parallel} , σ_{\perp} , σ_n) during magnetization rotation in the (103) plane. Symbols denote the results from DFT and TRS-Wannier calculations, while solid lines represent the fitted theoretical formulas ($\sigma_{\parallel} = \alpha + \beta \left(\frac{273}{400} + \frac{9}{100} \cos 2\psi + \frac{91}{400} \cos 4\psi \right)$, $\sigma_{\perp} = -\frac{\beta}{400} (18 \sin 2\psi + 91 \sin 4\psi)$, $\sigma_n = \frac{6}{25} \beta \sin^3 \psi$), with fitting parameters $\alpha = -896.116$ and $\beta = 100.928$ [S/cm]. σ_{\parallel} and σ_{\perp} agree well in periods and phases, whereas σ_n deviates around $\psi = 90^\circ$, indicating higher-order contributions.

3.3. Rank-resolved multipole and strain effects on IAHE in the (103) plane

3.3.1. Rank-wise contribution analysis in (103) plane

Next, by examining the contribution of each term in the multipole decomposition, we investigate which multipoles play dominant roles. Figure 13

summarizes the angle dependence of σ_{\parallel} , σ_{\perp} , and σ_n , for different truncations of the multipole decomposition. Considering only the lowest rank magnetic dipole M_1 , the parallel component σ_{\parallel} (Fig.13(a)) and perpendicular component σ_{\perp} (Fig.13(b)) well reproduce basic angular dependence of theoretical formulas given in Eqs. (19-21). Particularly, the out-of-plane component σ_n (Fig.13(c)) shows a $\sin^3 \psi$ shape with clear peak at $\psi = 90^\circ$. The M_1 -only case has better agreement with theoretical formulas, showing that M_1 has dominant contributions determining overall shape. The T_2 component is negligible and does not contribute to AHC.

When adding more ranks, higher-order components like M_3 , T_4 , and M_5 each have amplitudes comparable to M_1 and significantly modulate the angular dependence. As shown in Fig.13(d-f), adding M_3 and T_4 introduces new harmonic components to σ_{\parallel} and σ_{\perp} , and in the subsequent Fig.13(g-i), adding M_5 and T_6 contributions causes these harmonic components to cancel each other, finally converging to the overall shape. This cancellation effect reduces amplitudes compared to the M_1 alone case, while causing fine deviations from theoretical curves for σ_n and changes in peak shapes around $\psi = 90^\circ$. Especially in Fig. 13(d-f), we identify the rank-4 magnetic-toroidal component T_4 as providing a large contribution with the sign opposite to the others.

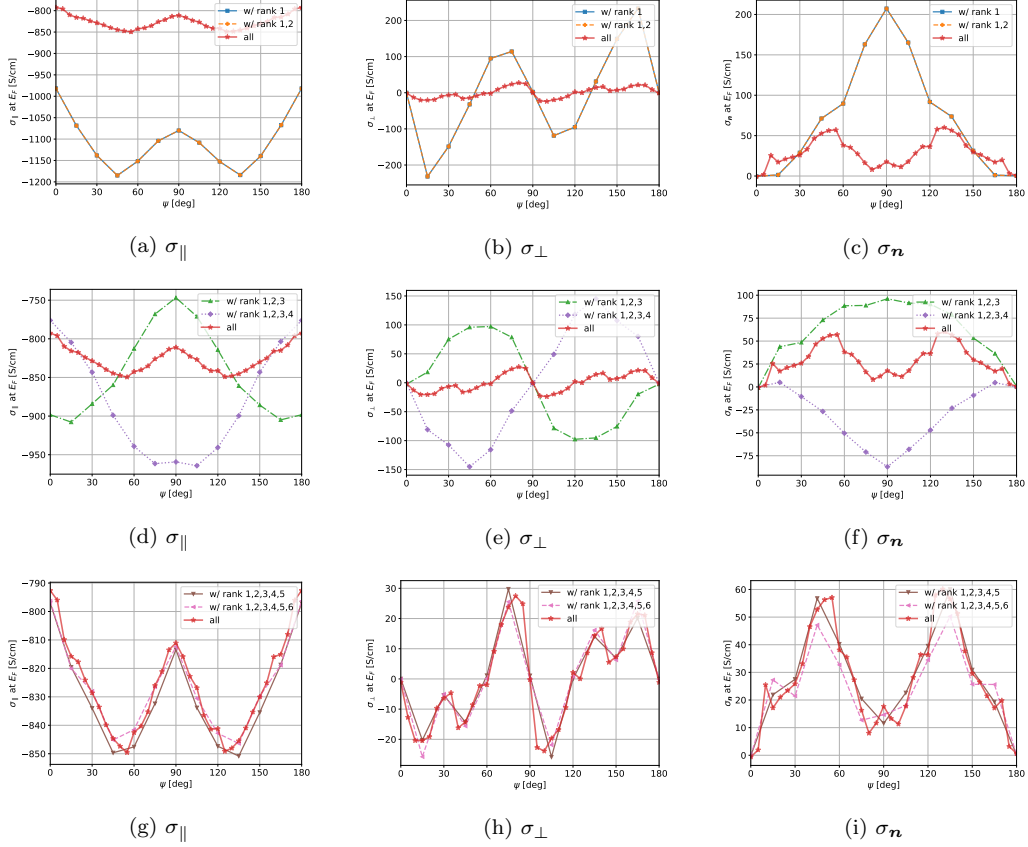


Figure 13: Angular dependence of σ_{\parallel} (a,d,g), σ_{\perp} (b,e,h) and σ_n (c,f,i) for different truncations of the multipole decomposition: (a-c) results including multipoles up to rank 1 and 2, (d-f) up to rank 3 and 4, (g-i) up to rank 5 and 6. Results including all ranks are also shown as references.

Figure 14 shows the angular dependence obtained by considering only one of \mathbb{M}_3 , \mathbb{T}_4 , or \mathbb{M}_5 as the terms corresponding to magnetization, H^a . Consistent with the cumulative analysis in Fig. 13, single-rank rotations of \mathbb{M}_3 , \mathbb{T}_4 , and \mathbb{M}_5 reproduce similar trends, such that \mathbb{T}_4 contributes with the opposite sign and reshapes the valley of σ_n near $\psi = 90^\circ$ (Fig. 14(c)). The next subsection examines prospects for controlling \mathbb{T}_4 .

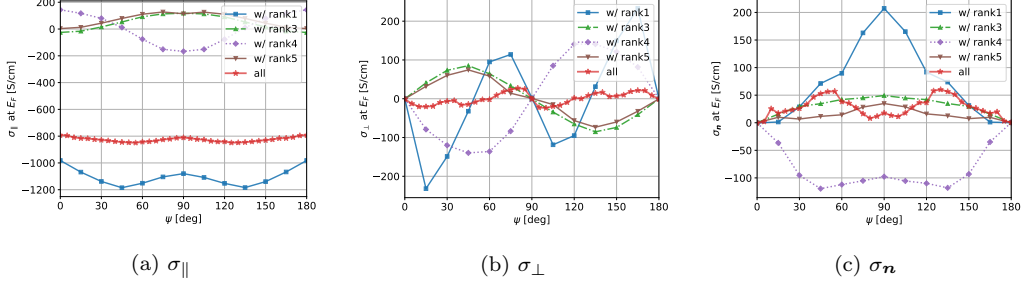


Figure 14: Angular dependence of AHC components (σ_{\parallel} , σ_{\perp} , σ_n) during magnetization rotation in the (103) plane, comparing cases where only single ranks such as M_1 , M_3 , T_4 , or M_5 are included. Consistent with Fig. 13, the rank-4 magnetic-toroidal component T_4 contributes to the AHC with the opposite sign to M_1 , M_3 , and M_5 and reshapes σ_n around $\psi = 90^\circ$.

3.3.2. Strain-induced symmetry lowering and IAHE modulation in the (103) plane

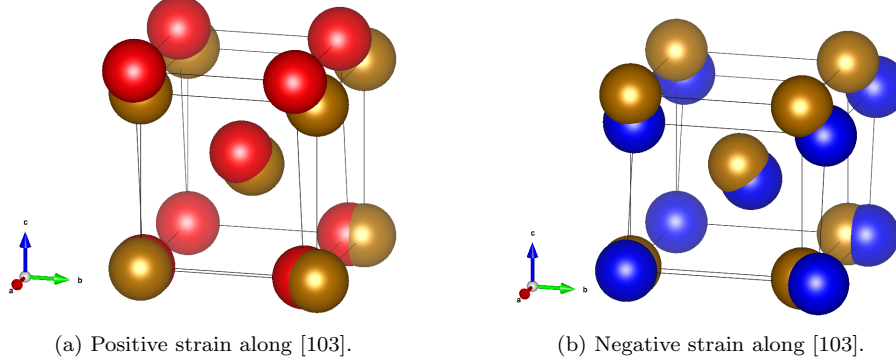


Figure 15: Crystal structures of body-centered cubic iron (bcc Fe) with positive strain and with negative strain along the [103] direction.

We consider a body-centered cubic crystal subjected to a uniform, volume-conserving strain along the [103] direction (Fig. 15). Let \mathbf{a}_i denote the original lattice vectors and \mathbf{a}'_i the deformed ones. They are related by the deformation gradient F as

$$\mathbf{a}'_i = F \mathbf{a}_i, \quad (38)$$

$$F = \lambda^{-1/2} I + (\lambda - \lambda^{-1/2})(\mathbf{n} \otimes \mathbf{n}), \quad (39)$$

where I is the identity tensor, λ is the stretch ratio, and \mathbf{n} is a unit vector specifying the strain direction, that is, $\mathbf{n} = \frac{1}{\sqrt{10}}(1, 0, 3)$.

Under this strain, the point group of the system is reduced from O_h to C_{2h} . Table 2 summarizes the correspondence between multipoles and irreducible representations in O_h and C_{2h} . From the table, M_z , M_z^α , and T_z^α , which belong to T_{1g} in O_h , transform as A_g in C_{2h} . This reduction indicates that, in C_{2h} , many other magnetic and magnetic-toroidal multipoles in A_g become active and may contribute to the AHC.

Table 2: Multipoles and irreducible representations in O_h and C_{2h} point groups. Excerpted from Ref. [49].

\mathbb{M}	\mathbb{T}	O_h	C_{2h}
–	T_0, T_4	A_{1g}	A_g
M_{xyz}	–	A_{2g}	A_g
–	T_u, T_{4u}	E_g	A_g
–	T_v, T_{4v}	E_g	A_g
M_x, M_x^α	T_{4x}^α	T_{1g}	B_g
M_y, M_y^α	T_{4y}^α	T_{1g}	B_g
M_z, M_z^α	T_{4z}^α	T_{1g}	A_g
M_x^β	T_{yz}, T_{4x}^β	T_{2g}	B_g
M_y^β	T_{zx}, T_{4y}^β	T_{2g}	B_g
M_z^β	T_{xy}, T_{4z}^β	T_{2g}	A_g

Figure 16 shows the angular dependence of the out-of-plane AHC component σ_n during magnetization rotation in the (103) plane, under both tensile (positive) and compressive (negative) strains along [103]. In both cases, the peak structure around $\psi = 90^\circ$ is significantly altered compared to the unstrained case (Fig. 12(c)). Under compressive strain, the valley-like feature around $\psi = 90^\circ$ becomes relatively weaker. In contrast, tensile strain deepens this valley, and at +1% strain, the sign of σ_n is inverted for all angles ψ . This indicates that strain enhances the weight of A_g channels such as T_4 , which contributes with the opposite sign, thereby deepening the valley and inverting the sign of σ_n over the entire angular range.

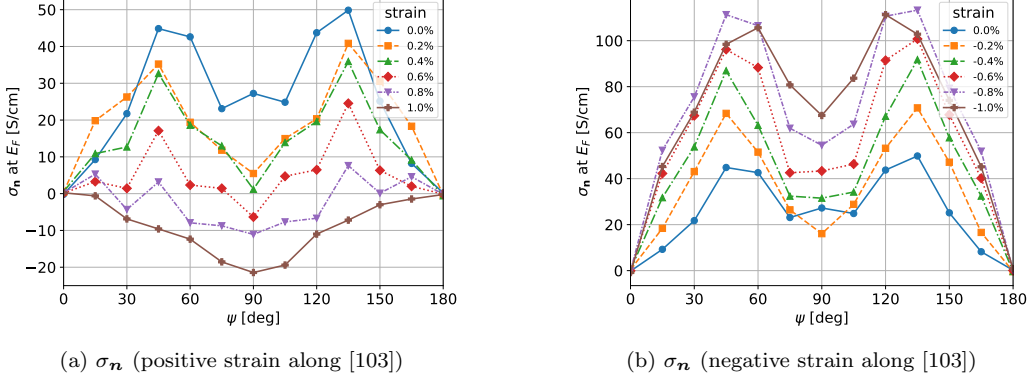


Figure 16: Effect of uniaxial strain applied along [103] on the out-of-plane AHC component σ_n during magnetization rotation in the (103) plane. (a) tensile (positive) strain; (b) compressive (negative) strain.

3.4. Minimal two-orbital p_z - d_{xy} model Hamiltonian

To understand the strain effect on the angular dependence of the IAHE, we propose a minimal model Hamiltonian that reproduces the valley-like IAHE response in the (103) plane. The Hamiltonian consists of five terms—on-site energy H_{on} , nearest-neighbor hopping H_{hop} , exchange interaction H_{ex} , and magnetic-toroidal hopping on first- and second-nearest-neighbor bonds, $H_{\text{MT}}^{(1)}$ and $H_{\text{MT}}^{(2)}$, explicitly written as,

$$H = H_{\text{on}} + H_{\text{hop}} + H_{\text{ex}} + H_{\text{MT}}^{(1)} + H_{\text{MT}}^{(2)}, \quad (40)$$

$$H_{\text{on}} = \sum_i \Psi_i^\dagger \left[\varepsilon_0 \tau_0 \otimes s_0 + \frac{\Delta_0}{2} \tau_z \otimes s_0 \right] \Psi_i, \quad (41)$$

$$H_{\text{hop}} = t_0 \sum_{\langle ij \rangle} \Psi_i^\dagger [\tau_0 \otimes s_0] \Psi_j, \quad (42)$$

$$H_{\text{ex}} = -\Delta \sum_i \Psi_i^\dagger [\tau_0 \otimes \hat{\mathbf{M}}(\psi) \cdot \mathbf{s}] \Psi_i, \quad (43)$$

$$H_{\text{MT}}^{(1)} = -it_{\text{T}}^{(1)} \sum_{\langle ij \rangle} \Psi_i^\dagger [\tau_y \otimes (\hat{\mathbf{M}}(\psi) \times \mathbf{s}) \cdot \mathbf{d}_{ij}] \Psi_j + \text{h.c.}, \quad (44)$$

$$H_{\text{MT}}^{(2)} = -it_{\text{T}}^{(2)} \sum_{\langle\langle ij \rangle\rangle} \Psi_i^\dagger [\tau_y \otimes (\hat{\mathbf{M}}(\psi) \times \mathbf{s}) \cdot \mathbf{d}_{ij}] \Psi_j + \text{h.c..} \quad (45)$$

Here, $\Psi_i = (p_{z,i\uparrow}, p_{z,i\downarrow}, d_{xy,i\uparrow}, d_{xy,i\downarrow})$ collects the p_z - and d_{xy} -orbital operators. The Pauli matrices $(\tau_0, \tau_x, \tau_y, \tau_z)$ and (s_0, s_x, s_y, s_z) act in orbital and spin

space, respectively. $\hat{\mathbf{M}}(\psi)$ is the unit vector specifying the magnetization direction, \mathbf{d}_{ij} is the displacement vector from site i to site j , and $\langle ij \rangle$ and $\langle\langle ij \rangle\rangle$ denote first-nearest-neighbor and second-nearest-neighbor pairs with body-centered cubic structure, respectively. We set $\varepsilon_0 = 0$, $\Delta_0 = 1.0$, $t_0 = -1.0$, and $\Delta = 1.0$, and vary $t_T^{(1)} \in [0, 0.2]$ and $t_T^{(2)} \in [0, 0.14]$.

Figure 17 shows the angular dependence of the out-of-plane AHC component σ_n during magnetization rotation in the (103) plane, calculated using the minimal model Hamiltonian. In Fig. 17(a), we vary the first-nearest-neighbor magnetic-toroidal hopping $t_T^{(1)}$ with $t_T^{(2)} = 0$, whereas in Fig. 17(b), we vary the second-nearest-neighbor magnetic-toroidal hopping $t_T^{(2)}$ with $t_T^{(1)} = 0.2$. From Fig. 17(a), we find that σ_n vanishes at $t_T^{(1)} = 0$ and increases in magnitude with $t_T^{(1)}$, without changing its overall shape. By contrast, Fig. 17(b) shows that increasing $t_T^{(2)}$ deepens the valley of σ_n around $\psi = 90^\circ$. This indicates that second-nearest-neighbor magnetic-toroidal hopping is the primary driver of the valley-like profile in σ_n .

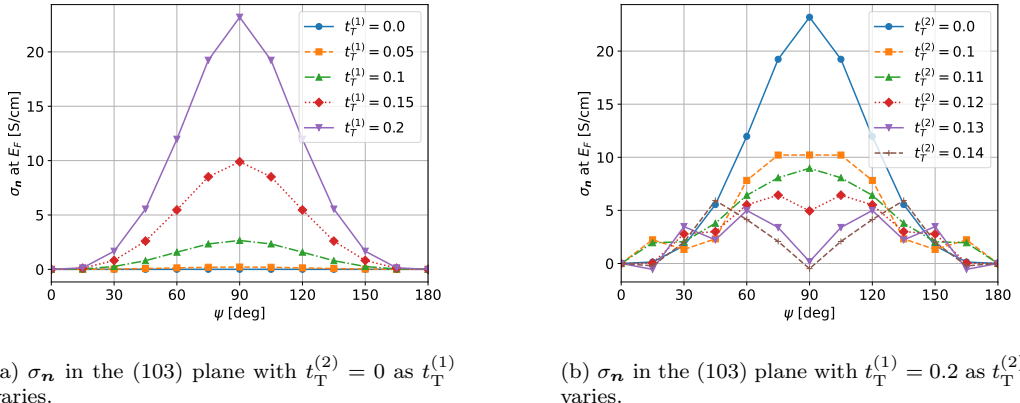


Figure 17: Out-of-plane AHC σ_n during magnetization rotation in the (103) plane: (a) for $t_T^{(1)} \in [0, 0.2]$ with $t_T^{(2)} = 0$; (b) for $t_T^{(2)} \in [0, 0.14]$ with $t_T^{(1)} = 0.2$.

4. Discussion

This study demonstrates that the TRS-Wannier framework for magnetization rotation is effective not only for calculating magnetic anisotropy energy, as shown in the previous study [36], but also for analyzing AHE anisotropy. By combining this framework with multipole decomposition using SAMB, we demonstrate that the symmetry of the resulting Hamiltonians

can be quantitatively evaluated. Complete SAMB decomposition typically requires millions of basis matrices, which makes the interpretation of individual multipole components challenging. Nevertheless, the decomposition coefficients can serve as fingerprints unique to each material and magnetic ordering, with potential applications as descriptors in machine learning.

Notably, significant contributions from higher-order magnetic and magnetic toroidal multipoles appear not only in systems with f -electrons, such as UNi_4B [50, 51, 52, 53], Ce_3TiBi_5 [54, 55, 56, 57], but also in the seemingly simple bcc Fe. In particular, we quantitatively demonstrate that high-rank components—including magnetic octupoles, magnetic toroidal 16-poles, and magnetic 32-poles—can contribute with strengths comparable to those of magnetic dipoles. We further find that the contribution from magnetic toroidal 16-poles acts with the opposite sign relative to the other dominant terms. These findings indicate that the deviations from the angular formulas, which are derived from an expansion in the magnetization direction based on the spin group theory, call for the inclusion of higher-order multipolar terms and/or an explicit treatment of orbital magnetization arising from magnetic-toroidal hopping processes that simultaneously change spin and orbital states.

Building on this observation, we show that applying strain can control the magnetic-toroidal 16-pole contribution and even reverse the sign of the IAHE. These results establish magnetoelastic engineering as a viable strategy to manipulate high-order multipoles in ferromagnets and may offer a promising route toward spintronics applications, where tunable AHC magnitude and angular dependence can be exploited for device design.

5. Conclusion

We have introduced a microscopic framework that combines time-reversal symmetric Wannier functions with a symmetry-adapted multipole basis to analyze the in-plane anomalous Hall effect in ferromagnets. By decomposing first-principles Hamiltonians into multipole components and rotating magnetization rank by rank, the method quantifies symmetry fidelity and identifies the channels that control the angular dependence of the conductivity. Applied to body-centered cubic iron, it reproduces the angle dependence from density functional theory and shows that high-rank magnetic and magnetic toroidal multipoles are comparable in magnitude to magnetic dipoles and shape the valley-like response. Uniaxial strain along the [103] direction lowers

symmetry, opens additional magnetic toroidal channels, and enables tunable reshaping of the angular response, including complete sign inversion under modest tensile strain. These results establish multipole-resolved Hamiltonian engineering as a practical route to predict and control the in-plane anomalous Hall effect and point to magnetoelastic strategies for tunable spintronic functionality in simple ferromagnets.

6. Code availability

The codes and data will be made available upon request.

7. Acknowledgement

This work was supported by JSPS KAKENHI Grant No. 22K03447, and 23H04869, JST-Mirai Program (JPMJMI20A1), JST-ASPIRE (JPM-JAP2317), Center for Science and Innovation in Spintronics (CSIS), Tohoku University and GP-Spin at Tohoku University.

References

- [1] N. Nagaosa, J. Sinova, S. Onoda, A. H. MacDonald, N. P. Ong, Anomalous hall effect, *Rev. Mod. Phys.* 82 (2) (2010) 1539–1592. doi:10.1103/RevModPhys.82.1539.
- [2] D. Xiao, M.-C. Chang, Q. Niu, Berry phase effects on electronic properties, *Rev. Mod. Phys.* 82 (3) (2010) 1959–2007. doi:10.1103/RevModPhys.82.1959.
- [3] H. Chen, Q. Niu, A. H. MacDonald, Anomalous hall effect arising from noncollinear antiferromagnetism, *Phys. Rev. Lett.* 112 (1) (2014) 017205. doi:10.1103/PhysRevLett.112.017205.
- [4] S. Nakatsuji, N. Kiyohara, T. Higo, Large anomalous hall effect in a non-collinear antiferromagnet at room temperature, *Nature* 527 (7577) (2015) 212–215. doi:10.1038/nature15723.
- [5] A. K. Nayak, J. E. Fischer, Y. Sun, B. Yan, J. Karel, A. C. Komarek, C. Shekhar, N. Kumar, W. Schnelle, J. Kübler, C. Felser, S. S. P. Parkin, Large anomalous hall effect driven by a nonvanishing berry curvature in the noncollinear antiferromagnet Mn₃Ge, *Sci. Adv.* 2 (4) (2016) e1501870. doi:10.1126/sciadv.1501870.

- [6] M. Ikhlas, T. Tomita, T. Koretsune, M.-T. Suzuki, D. Nishio-Hamane, R. Arita, Y. Otani, S. Nakatsuji, Large anomalous nernst effect at room temperature in a chiral antiferromagnet, *Nat. Phys.* 13 (11) (2017) 1085–1090. doi:10.1038/nphys4181.
- [7] Y. Zhang, Y. Sun, H. Yang, J. Železný, S. P. P. Parkin, C. Felser, B. Yan, Strong anisotropic anomalous hall effect and spin hall effect in the chiral antiferromagnetic compounds Mn_3X ($X=Ge, sn, ga, ir, rh, and pt$), *Phys. Rev. B.* 95 (7) (2017). doi:10.1103/PhysRevB.95.075128.
- [8] H. Yang, Y. Sun, Y. Zhang, W.-J. Shi, S. S. P. Parkin, B. Yan, Topological weyl semimetals in the chiral antiferromagnetic materials Mn_3Ge and Mn_3Sn , *New J. Phys.* 19 (1) (2017) 015008. doi:10.1088/1367-2630/aa5487.
- [9] M.-T. Suzuki, T. Koretsune, M. Ochi, R. Arita, Cluster multipole theory for anomalous hall effect in antiferromagnets, *Phys. Rev. B Condens. Matter* 95 (9) (2017) 094406. doi:10.1103/PhysRevB.95.094406.
- [10] Z. Liu, G. Zhao, B. Liu, Z. F. Wang, J. Yang, F. Liu, Intrinsic quantum anomalous hall effect with in-plane magnetization: Searching rule and material prediction, *Phys. Rev. Lett.* 121 (24) (2018) 246401. doi:10.1103/PhysRevLett.121.246401.
- [11] K. Zhao, T. Hajiri, H. Chen, R. Miki, H. Asano, P. Gegenwart, Anomalous hall effect in the noncollinear antiferromagnetic antiperovskite $Mn_3Ni_{1-x}Cu_xN$, *Phys. Rev. B.* 100 (4) (2019). doi:10.1103/PhysRevB.100.045109.
- [12] T. Chen, T. Tomita, S. Minami, M. Fu, T. Koretsune, M. Kitatani, I. Muhammad, D. Nishio-Hamane, R. Ishii, F. Ishii, R. Arita, S. Nakatsuji, Anomalous transport due to weyl fermions in the chiral antiferromagnets Mn_3X , $x = sn, ge$, *Nat. Commun.* 12 (1) (2021) 572. doi:10.1038/s41467-020-20838-1.
- [13] M. Naka, S. Hayami, H. Kusunose, Y. Yanagi, Y. Motome, H. Seo, Anomalous hall effect in κ -type organic antiferromagnets, *Phys. Rev. B.* 102 (7) (2020). doi:10.1103/PhysRevB.102.075112.

- [14] L. Šmejkal, A. H. MacDonald, J. Sinova, S. Nakatsuji, T. Jungwirth, Anomalous hall antiferromagnets, *Nature Reviews Materials* 7 (6) (2022) 482–496. doi:10.1038/s41578-022-00430-3.
- [15] H. Reichlova, R. Lopes Seeger, R. González-Hernández, I. Kounta, R. Schlitz, D. Kriegner, P. Ritzinger, M. Lammel, M. Leiviskä, A. Birk Hellenes, K. Olejník, V. Petříček, P. Doležal, L. Horak, E. Schmoranzerova, A. Badura, S. Bertaina, A. Thomas, V. Baltz, L. Michez, J. Sinova, S. T. B. Goennenwein, T. Jungwirth, L. Šmejkal, Observation of a spontaneous anomalous hall response in the Mn_5Si_3 d-wave altermagnet candidate, *Nat. Commun.* 15 (1) (2024) 1–10. doi:10.1038/s41467-024-48493-w.
- [16] R. Takagi, R. Hirakida, Y. Settai, R. Oiwa, H. Takagi, A. Kitaori, K. Yamuchi, H. Inoue, J.-I. Yamaura, D. Nishio-Hamane, S. Itoh, S. Aji, H. Saito, T. Nakajima, T. Nomoto, R. Arita, S. Seki, Spontaneous hall effect induced by collinear antiferromagnetic order at room temperature, *Nat. Mater.* (2024) 1–6doi:10.1038/s41563-024-02058-w.
- [17] X. Liu, J. K. Furdyna, M. Dobrowolska, W. L. Lim, C. Xie, Y. J. Cho, Unique properties of magnetotransport in GaMnAs films grown on vicinal and high-index planes, *J. Phys. Condens. Matter* 19 (16) (2007) 165205. doi:10.1088/0953-8984/19/16/165205.
- [18] E. Roman, Y. Mokrousov, I. Souza, Orientation dependence of the intrinsic anomalous hall effect in hcp cobalt, *Phys. Rev. Lett.* 103 (9) (2009) 097203. doi:10.1103/PhysRevLett.103.097203.
- [19] H. Tan, Y. Liu, B. Yan, Unconventional anomalous hall effect from magnetization parallel to the electric field, *Phys. Rev. B.* 103 (21) (2021). doi:10.1103/PhysRevB.103.214438.
- [20] J. Zhou, W. Zhang, Y. Lin, J. Cao, Y. Zhou, W. Jiang, H. Du, B. Tang, J. Shi, B. Jiang, X. Cao, B. Lin, Q. Fu, C. Zhu, W. Guo, Y. Huang, Y. Yao, S. Parkin, J. Zhou, Y. Gao, Y. Wang, Y. Hou, Y. Yao, K. Sue-naga, X. Wu, Z. Liu, Heterodimensional superlattice with in-plane anomalous hall effect, *Nature* 609 (2022) 46–51. doi:10.1038/s41586-022-05031-2.

- [21] J. Cao, W. Jiang, X.-P. Li, D. Tu, J. Zhou, J. Zhou, Y. Yao, In-plane anomalous hall effect in PT-symmetric antiferromagnetic materials, *Phys. Rev. Lett.* 130 (16) (2023) 166702. doi:10.1103/PhysRevLett.130.166702.
- [22] T. Kurumaji, Symmetry-based requirement for the measurement of electrical and thermal hall conductivity under an in-plane magnetic field, *Phys. Rev. Res.* 5 (2) (2023). doi:10.1103/PhysRevResearch.5.023138.
- [23] A. Nakamura, S. Nishihaya, H. Ishizuka, M. Kriener, Y. Watanabe, M. Uchida, In-plane anomalous hall effect associated with orbital magnetization: Measurements of low-carrier density films of a magnetic weyl semimetal, *Phys. Rev. Lett.* 133 (23) (2024) 236602. doi:10.1103/PhysRevLett.133.236602.
- [24] W. Miao, B. Guo, S. Stemmer, X. Dai, Engineering the in-plane anomalous hall effect in Cd_3As_2 thin films, *Phys. Rev. B.* 109 (15) (2024). doi:10.1103/PhysRevB.109.155408.
- [25] W. Peng, Z. Liu, H. Pan, P. Wang, Y. Chen, J. Zhang, X. Yu, J. Shen, M. Yang, Q. Niu, Y. Gao, D. Hou, Observation of the in-plane anomalous hall effect induced by octupole in magnetization space, arXiv [cond-mat.mtrl-sci] (2024). doi:10.48550/arXiv.2402.15741.
- [26] S. Nishihaya, Y. Matsuki, H. Kaminakamura, H. Sugeno, M.-C. Jiang, Y. Murakami, R. Arita, H. Ishizuka, M. Uchida, Spontaneous in-plane anomalous hall response observed in a ferromagnetic oxide, *Adv. Mater.* (e02624) (2025) e02624. doi:10.1002/adma.202502624.
- [27] L. Wang, G. Tian, H. Chen, J. Zhao, H. Shi, H. Wang, Z. Li, X. Wu, In-plane hall effect in $\text{Co}_3\text{Sn}_2\text{S}_2$, *Phys. Rev. B.* 111 (5) (2025). doi:10.1103/PhysRevB.111.054412.
- [28] Z. Liu, M. Wei, W. Peng, D. Hou, Y. Gao, Q. Niu, Multipolar anisotropy in anomalous hall effect from spin-group symmetry breaking, *Phys. Rev. X.* 15 (3) (2025). doi:10.1103/PhysRevX.15.031006.
- [29] I. Souza, N. Marzari, D. Vanderbilt, Maximally localized wannier functions for entangled energy bands, *Phys. Rev. B Condens. Matter* 65 (3) (2001) 035109. doi:10.1103/PhysRevB.65.035109.

- [30] N. Marzari, D. Vanderbilt, Maximally localized generalized wannier functions for composite energy bands, *Phys. Rev. B Condens. Matter* 56 (20) (1997) 12847–12865. doi:10.1103/PhysRevB.56.12847.
- [31] J. Qiao, G. Pizzi, N. Marzari, Projectability disentanglement for accurate and automated electronic-structure hamiltonians, *Npj Comput. Mater.* 9 (1) (2023) 208. doi:10.1038/s41524-023-01146-w.
- [32] T. Ozaki, Closest wannier functions to a given set of localized orbitals, *Phys. Rev. B.* 110 (12) (2024) 125115. doi:10.1103/PhysRevB.110.125115.
- [33] R. Oiwa, A. Inda, S. Hayami, T. Nomoto, R. Arita, H. Kusunose, Symmetry-adapted closest wannier modeling based on complete multipole basis set, *Phys. Rev. B.* 112 (3) (2025). doi:10.1103/2s5q-p42x.
- [34] R. Sakuma, Symmetry-adapted wannier functions in the maximal localization procedure, *Phys. Rev. B Condens. Matter* 87 (23) (2013) 235109. doi:10.1103/PhysRevB.87.235109.
- [35] T. Koretsune, Construction of maximally-localized wannier functions using crystal symmetry, *Comput. Phys. Commun.* 285 (2023) 108645. doi:10.1016/j.cpc.2022.108645.
- [36] H. Saito, T. Koretsune, Efficient calculation of magnetocrystalline anisotropy energy using symmetry-adapted wannier functions, *Comput. Phys. Commun.* 305 (109325) (2024) 109325. doi:10.1016/j.cpc.2024.109325.
- [37] H. Kusunose, R. Oiwa, S. Hayami, Symmetry-adapted modeling for molecules and crystals, *Phys. Rev. B Condens. Matter* 107 (19) (2023) 195118. doi:10.1103/PhysRevB.107.195118.
- [38] A. Inda, R. Oiwa, S. Hayami, H. M. Yamamoto, H. Kusunose, Quantification of chirality based on electric toroidal monopole, *J. Chem. Phys.* 160 (18) (2024) 184117. doi:10.1063/5.0204254.
- [39] S. Hayami, H. Kusunose, Unified description of electronic orderings and cross correlations by complete multipole representation, *J. Phys. Soc. Jpn.* 93 (7) (2024). doi:10.7566/JPSJ.93.072001.

- [40] R. Oiwa, H. Kusunose, Predominant electronic order parameter for structural chirality: Role of spinless electronic toroidal multipoles in Te and Se, *Phys. Rev. Res.* 7 (3) (2025). doi:10.1103/1zq8-pqh8.
- [41] H. Kusunose, R. Oiwa, S. Hayami, Complete multipole basis set for single-centered electron systems, *J. Phys. Soc. Jpn.* 89 (10) (2020) 104704. doi:10.7566/JPSJ.89.104704.
- [42] P. Liu, J. Li, J. Han, X. Wan, Q. Liu, Spin-group symmetry in magnetic materials with negligible spin-orbit coupling, *Phys. Rev. X.* 12 (2) (2022). doi:10.1103/PhysRevX.12.021016.
- [43] X. Chen, Y. Liu, P. Liu, Y. Yu, J. Ren, J. Li, A. Zhang, Q. Liu, Unconventional magnons in collinear magnets dictated by spin space groups, *Nature* 640 (8058) (2025) 349–354. doi:10.1038/s41586-025-08715-7.
- [44] P. Giannozzi, S. Baroni, N. Bonini, M. Calandra, R. Car, C. Cavazzoni, D. Ceresoli, G. L. Chiarotti, M. Cococcioni, I. Dabo, A. D. Corso, S. de Gironcoli, S. Fabris, G. Fratesi, R. Gebauer, U. Gerstmann, C. Gougaud, A. Kokalj, M. Lazzeri, L. Martin-Samos, N. Marzari, F. Mauri, R. Mazzarello, S. Paolini, A. Pasquarello, L. Paulatto, C. Sbraccia, S. Scandolo, G. Sclauzero, A. P. Seitsonen, A. Smogunov, P. Umari, R. M. Wentzcovitch, QUANTUM ESPRESSO: a modular and open-source software project for quantum simulations of materials, *J. Phys. Condens. Matter* 21 (39) (2009) 395502. doi:10.1088/0953-8984/21/39/395502.
- [45] P. Giannozzi, O. Andreussi, T. Brumme, O. Bunau, M. Buongiorno Nardelli, M. Calandra, R. Car, C. Cavazzoni, D. Ceresoli, M. Cococcioni, N. Colonna, I. Carnimeo, A. Dal Corso, S. de Gironcoli, P. Delugas, R. A. DiStasio, Jr, A. Ferretti, A. Floris, G. Fratesi, G. Fugallo, R. Gebauer, U. Gerstmann, F. Giustino, T. Gorni, J. Jia, M. Kawamura, H.-Y. Ko, A. Kokalj, E. Küçükbenli, M. Lazzeri, M. Marsili, N. Marzari, F. Mauri, N. L. Nguyen, H.-V. Nguyen, A. Otero-de-la Roza, L. Paulatto, S. Poncé, D. Rocca, R. Sabatini, B. Santra, M. Schlipf, A. P. Seitsonen, A. Smogunov, I. Timrov, T. Thonhauser, P. Umari, N. Vast, X. Wu, S. Baroni, Advanced capabilities for materials modelling with quantum ESPRESSO, *J. Phys. Condens. Matter* 29 (46) (2017) 465901. doi:10.1088/1361-648X/aa8f79.

- [46] J. P. Perdew, K. Burke, M. Ernzerhof, Generalized gradient approximation made simple, *Phys. Rev. Lett.* 77 (18) (1996) 3865–3868. doi:10.1103/PhysRevLett.77.3865.
- [47] A. Dal Corso, Pseudopotentials periodic table: From H to pu, *Comput. Mater. Sci.* 95 (2014) 337–350. doi:10.1016/j.commatsci.2014.07.043.
- [48] S. S. Tsirkin, High performance wannier interpolation of berry curvature and related quantities with WannierBerri code, *npj Comput Mater* 7 (1) (2021). doi:10.1038/s41524-021-00498-5.
- [49] S. Hayami, M. Yatsushiro, Y. Yanagi, H. Kusunose, Classification of atomic-scale multipoles under crystallographic point groups and application to linear response tensors, *Phys. Rev. B Condens. Matter* 98 (16) (2018) 165110. doi:10.1103/PhysRevB.98.165110.
- [50] S. A. Mentink, A. Drost, G. J. Nieuwenhuys, E. Frikkee, A. A. Menovsky, J. A. Mydosh, Magnetic ordering and frustration in hexagonal UNi₄B, *Phys. Rev. Lett.* 73 (7) (1994) 1031–1034. doi:10.1103/PhysRevLett.73.1031.
- [51] A. Oyamada, M. Kondo, K. Fukuoka, T. Itou, S. Maegawa, D. X. Li, Y. Haga, NMR studies of the partially disordered state in a triangular antiferromagnet UNi₄B, *J. Phys.: Condens. Matter* 19 (14) (2007) 145246. doi:10.1088/0953-8984/19/14/145246.
- [52] H. Saito, K. Uenishi, N. Miura, C. Tabata, H. Hidaka, T. Yanagisawa, H. Amitsuka, Evidence of a new current-induced magnetoelectric effect in a toroidal magnetic ordered state of UNi₄B, *J. Phys. Soc. Jpn.* 87 (3) (2018) 033702. doi:10.7566/JPSJ.87.033702.
- [53] T. Ishitobi, K. Hattori, Triple-Q partial magnetic orders induced by quadrupolar interactions: Triforce order scenario for UNi₄B, *Phys. Rev. B* 107 (10) (2023). doi:10.1103/PhysRevB.107.104413.
- [54] G. Motoyama, M. Sezaki, J. Gouchi, K. Miyoshi, S. Nishigori, T. Mutou, K. Fujiwara, Y. Uwatoko, Magnetic properties of new antiferromagnetic heavy-fermion compounds, Ce₃TiBi₅ and CeTi₃Bi₄, *Physica B Condens. Matter* 536 (2018) 142–144. doi:10.1016/j.physb.2017.10.005.

- [55] M. Shinozaki, G. Motoyama, M. Tsubouchi, M. Sezaki, J. Gouchi, S. Nishigori, T. Mutou, A. Yamaguchi, K. Fujiwara, K. Miyoshi, Y. Uwamoto, Magnetoelectric effect in the antiferromagnetic ordered state of Ce_3TiBi_5 with ce zig-zag chains, *J. Phys. Soc. Jpn.* 89 (3) (2020) 033703. doi:10.7566/JPSJ.89.033703.
- [56] M. Shinozaki, G. Motoyama, T. Mutou, S. Nishigori, A. Yamaguchi, K. Fujiwara, K. Miyoshi, A. Sumiyama, Study for current-induced magnetization in ferrotoroidal ordered state of Ce_3TiBi_5 , in: Proceedings of the International Conference on Strongly Correlated Electron Systems (SCES2019), *J. Phys. Soc. Jpn.*, 2020. doi:10.7566/JPSCP.30.011189.
- [57] S. Hayami, H. Kusunose, Magnetic toroidal moment under partial magnetic order in hexagonal zigzag-chain compound Ce_3TiBi_5 , *J. Phys. Soc. Jpn.* 91 (12) (2022). doi:10.7566/JPSJ.91.123701.